A comparison among FeF₃·3H₂O, FeF₃·0.33H₂O and FeF₃ cathode materials for lithium ion batteries: Structural, electrochemical, and mechanism studies

Li Liu*, Haipeng Guo, Meng Zhou, Qiliang Wei, Zhenhua Yang, Hongbo Shu, Xiukang Yang, Jinli Tan, Zichao Yan, Xianyou Wang*

School of Chemistry, Key Laboratory of Environmentally Friendly Chemistry and Applications of Ministry of Education, Xiangtan University, Xiangtan 411105, China

HIGHLIGHTS

- The properties comparison of FeF₃·3H₂O, FeF₃·0.33H₂O, and FeF₃ has been firstly investigated.
- The electrochemical reaction mechanism of FeF₃·3H₂O has been firstly studied.
- The electrochemical reaction mechanism of FeF₃·0.33H₂O also include conversion reaction has been firstly proved.
- FeF₃·0.33H₂O has the best electrochemical performance among these three iron fluorides has been demonstrated.

ARTICLE INFO

ABSTRACT

FeF₃·3H₂O, FeF₃·0.33H₂O, and FeF₃ have been synthesized via a liquid-phase method followed by heat treatment at different temperatures. The structure and performance of these iron fluorides have been characterized by X-ray diffraction (XRD), scanning electron microscopy (SEM), high-resolution transmission electron microscopy (HRTEM), selected-area electron diffraction (SAED), charge–discharge test, cyclic voltammetry (CV), electrochemical impedance spectroscopy (EIS) and galvanostatic intermittent titration technique (GITT). Though FeF₃·3H₂O, FeF₃·0.33H₂O, and FeF₃ have different crystalline structures, they can achieve the identical reversible electrochemical conversion reaction from Fe^{3+} to Fe^0 in the wide voltage range (1.0–4.5 V vs. Li⁺/Li). Among these three iron fluorides, FeF₃·0.33H₂O shows the best electrochemical performance. Moreover, ball milling with acetylene black combined with limiting cut-off voltage can further improve its electrochemical performance. FeF₃·0.33H₂O/C composite delivers excellent electrochemical performance in the voltage range of 2.0–4.5 V. Its capacity retentions remain as high as 83.8% and 83.3% after 100 cycles at 0.1 and 5 C, respectively. This study suggests a potential feasibility to prepare the optimal crystal structure of iron fluorides as high-performance cathode material for lithium-ion batteries.

1. Introduction

Global warming, modern city pollution, and finite fossil-fuel supplies sound the alarm for people to seek alternative energy sources and replacement of the internal combustion engines. Renewable energy sources (wind, tidal energy, wave, solar radiation) are unstable and diffuse in space, thus requiring energy storage. Among various available storage technologies, the lithium-ion battery is the most promising battery candidate to store chemical energy and deliver electrical energy with high conversion efficiency without gaseous emission.

As the dominant power source for electric vehicles and hybrid electric vehicles, rechargeable lithium batteries need to be further improved to compete with traditional petrol vehicles [1]. Therefore, intensive research efforts on searching for battery cathode materials with higher energy densities spring up. Traditional cathode materials, such as LiCoO₂, LiMn₂O₄, LiFePO₄, etc, have a limited actual specific capacity in the range of 120–160 mAh g⁻¹, which depend on Li⁺ intercalation/deintercalation that use only one unit valence change per cation. Recently, transition metal fluorides, such as CoF₂ [2], NiF₂ [3], CuF₂ [4] and FeF₃ [5–8] have been studied as a promising new class of cathode materials, which exhibit large

* Corresponding authors. Tel.: +86 731 58292206; fax: +86 731 58292477.
E-mail addresses: liulili1203@yahoo.com.cn, liulili1203@126.com (L. Liu), wxianyou@yahoo.com (X. Wang).

theoretical capacities and high discharge voltages due to their highly ionic metal–ligand bonds and small atomic weight. Unlike traditional compounds, transition metal fluorides, based on reversible conversion reaction, enable the full utilization of redox through the following reaction [5–11]:

$$MeF_n + nLi^+ + ne^- \rightleftarrows nLiF + Me \qquad (1)$$

Among these metal fluorides, iron(III) fluoride has recently become one of the most promising cathode materials for lithium ion batteries because of its high capacity and low cost.

The electrochemical reaction mechanism of FeF_3 with ReO_3-type structure has been proposed by Badway et al. [12–14], and two reactions are included

$$FeF_3 + Li + e^- \rightarrow LiFeF_3 \qquad (2)$$

$$LiFeF_3 + 2Li + 2e^- \rightarrow Fe^0 + 3LiF \qquad (3)$$

Reaction (2) has been found to be a conventional intercalation reaction, while reaction (3) is a conversion reaction. These two electrochemical reactions involve $3e^-$ transfer, so FeF_3 has a high theoretical specific capacity of 712 mAh g^{-1}. However, the high ionicity of FeF_3 combined with large bandgap results in electronically insulating behavior. In addition, LiF, the product of the conversion reaction, is also highly insulating. Therefore, FeF_3 has low actual capacity and fast capacity fading, and these shortcomings restrict its commercial applications. To overcome these problems, highly conductive carbon was used to improve the electrochemical activity of metal fluorides. Ball-milling FeF_3 with carbon, such as graphite, carbon black, and activated carbon could form FeF_3/C CMFNC (carbon metal fluoride nanocomposites) which shows an initial discharge capacity of about 170 mAh g^{-1} in the range of 2.0–4.5 V and highest initial discharge capacity of 202 mAh g^{-1} in the range of 2.5–4.5 V based on the weight of nanocomposite material at a low current density of 7.58 mA g^{-1} at 22 °C, respectively. Furthermore, FeF_3/C can achieve a reversible specific capacity of 367 mAh g^{-1} at 22 °C and 660 mAh g^{-1} at 70 °C in the range of 1.5–4.5 V at 7.58 mA g^{-1} [12]. Though FeF_3/C CMFNC has high specific capacity, the cycle stability of these composites is very poor. Li et al. prepared the FeF_3/C by ball-milling the as-prepared FeF_3 nanocrystals with graphite [8]. The FeF_3/C nanocomposites show a high reversible specific capacity of about 700 mAh g^{-1} in the range of 1.0–4.5 V, but the short cycling test with only 10 cycles were performed.

Iron(III) fluoride with trace amounts of hydration water ($FeF_3 \cdot 0.33H_2O$) is regarded as a novel cathode material, which even has better electrochemical performance than anhydrous FeF_3 [15–21]. Li et al. synthesized $FeF_3 \cdot 0.33H_2O$ with a unique one-dimensional tunnel by using the low-temperature ionic-liquid-based synthesis method [15–17]. The discharge capacity of $FeF_3 \cdot 0.33H_2O$ was 153 mAh g^{-1} at the sixth cycle and decreased to 130 mAh g^{-1} after 30 cycles at a current density of 14 mA g^{-1} [17]. Notably, the single-wall carbon nanotube (SWNT)-$FeF_3 \cdot 0.33H_2O$ composite material exhibited remarkable rate performances (220 mAh g^{-1} at 0.1 °C and 80 mAh g^{-1} at 10 °C, 1 C = 237 mA g^{-1}) and better cycle performance (143 mAh g^{-1} at 0.1 °C after 30 cycles) in the voltage of 1.7–4.5 V at room temperature [16]. What's more, the prepared $FeF_3 \cdot 0.33H_2O/MoS_2$ [18], $FeF_3 \cdot 0.33H_2O/V_2O_5$ [19], and $FeF_3 \cdot 0.33H_2O/ACMB$ (active carbon microbead) [20], which have been reported by our team, showed promising results. Recently, we successfully synthesized Co-doped $FeF_3 \cdot 0.33H_2O$ and found that cation doping was an effective method to improve the electrochemical performance [21]. The structure and electrochemical reaction mechanism of $FeF_3 \cdot 0.33H_2O$ have also been investigated by

Li et al. [15–17]. They thought that in contrast to ReO_3-type FeF_3 which was based on a conversion reaction, $FeF_3 \cdot 0.33H_2O$ was based on a solid-solution behavior in the voltage of 1.6–4.5 V [15–17]. Though the conversion reaction didn't occur above 1.6 V, the reaction mechanism below 1.6 V was not studied and unclear.

Another iron(III) fluoride with three hydration water ($FeF_3 \cdot 3H_2O$) was reported as another novel cathode material for lithium ion battery in the voltage of 2.0–4.5 V recently [22]. However, the $FeF_3 \cdot 3H_2O/C$ prepared by ball-milling $FeF_3 \cdot 3H_2O$ with acetylene black only achieved a maximum discharge capacity of 112 mA g^{-1} [22]. Moreover, the electrochemical reaction mechanism of $FeF_3 \cdot 3H_2O$ is totally unknown.

In this work, we synthesized three kinds of iron fluoride compounds with different hydration water ($FeF_3 \cdot 3H_2O$, $FeF_3 \cdot 0.33H_2O$, and FeF_3). They were synthesized via a liquid-phase method followed by heat treatment at different temperatures. Then the corresponding $FeF_3 \cdot 3H_2O/C$, $FeF_3 \cdot 0.33H_2O/C$ and FeF_3/C nanocomposites were obtained by mechanical ball-milling with conductive acetylene black (AB) powders and heat-treated in different conditions. The crystal structure, morphology, electrochemical performance, and kinetic properties of synthesized iron fluoride nanocomposites were investigated systematically. We concentrate on discussing the reaction mechanism and structural evolution during the discharge/charge process of $FeF_3 \cdot 3H_2O/C$, $FeF_3 \cdot 0.33H_2O/C$, FeF_3/C nanocomposites by cyclic voltammetry (CV) and X-ray diffraction (XRD) in the voltage of 1.0–4.5 V. Especially, their electrochemical performances as cathode materials at room temperature in the range of 2.0–4.5 V were compared in detail. This study aims to explore the optimal crystal structure of iron trifluoride as high-performance cathode material for lithium ion batteries.

2. Experimental section

2.1. Preparation of materials

$FeF_3 \cdot 3H_2O$, $FeF_3 \cdot 0.33H_2O$, and FeF_3 were prepared by a simple liquid-phase method. Firstly, 10% excess mass of stoichiometric NaOH solution was added slowly to the solution which contained $FeCl_3$ under vigorous stirring to form $Fe(OH)_3$ precipitations, then the precipitations were aged for 12 h, washed twice by anhydrous alcohol and separated by filtration, followed by drying at 80 °C for 10 h in air to remove redundant water. Secondly, excessive HF aqueous solution (40 wt.%) was added to the above precipitation in a sealed teflon wares, with continued stirring for 4 h at 30 °C to form a uniform pink liquid, then the solution was continuously agitated at 80 °C for 12 h, until the precipitates were completely formed. Finally, the residual HF and water were eliminated by heating in air and the residue was dried at 80 °C for 19 h in a vacuum drying oven, thus obtained pink $FeF_3 \cdot 3H_2O$ precursor. Next, reseda $FeF_3 \cdot 0.33H_2O$ and brown FeF_3 compounds were obtained by heat treatment at 180 °C for 12 h and 400 °C for 2 h in a tube furnace with argon flow, respectively.

The $FeF_3 \cdot 3H_2O/C$, $FeF_3 \cdot 0.33H_2O/C$ and FeF_3/C nanocomposites were obtained by ball-milling the as-prepared $FeF_3 \cdot 3H_2O$, $FeF_3 \cdot 0.33H_2O$ and FeF_3 with acetylene black (AB) in air at 320 rpm for 3 h (weight ratio of iron fluoride: AB = 85:15). Finally, the prepared $FeF_3 \cdot 3H_2O/C$, $FeF_3 \cdot 0.33H_2O/C$ were dried at 75 °C for 5 h, 170 °C for 3 h in a vacuum drying oven, while FeF_3/C was heated at a rate of 5 °C min^{-1} until reaching 350 °C without the temperature holding step in a tube furnace with argon flow to obtain the final composites.

2.2. Structure, characterization and electrochemical measurements

The precursor was analyzed by thermogravimetry (TG) using a Thermogravimetric-differential Thermal analyzer (Standard Type

High temp. Type, Rigaku). The differential scanning calorimetry (DSC) measurements of the precursor were carried out in a DSC 200 PC with a heating rate of 10 °C min^{-1} in N$_2$ atmosphere.

The structures of the synthesized samples were characterized by X-ray diffraction. X-ray powder diffraction data were obtained using a Rigaku D/MAX-2500 powder diffractometer with a graphite monochromatic and Cu Kα radiation ($k = 0.15418$ nm) operated at a scan rate of 4 °min^{-1} in the 2θ range of 10–80°.

Scanning electron microscope (SEM) images of the sample were collected using a JEOL JSM-6610 scanning electron microscope. High-resolution transmission electron microscopy (HRTEM) and selected-area electron diffraction (SAED) measurements were carried out using a JEOL JEM-2100F transmission electron microscope at an acceleration voltage of 200 kV.

The cathodes for lithium cells were fabricated by mixing the cathode material, carbon black, and polyvinylidene fluoride (PVDF) binder with a weight ratio of 80:10:10 in N-methyl pyrrolidinone, which were then pasted on aluminum foil followed by drying under vacuum at 70 °C for 24 h. The testing cells were assembled with the cathodes thus fabricated, metallic lithium anode, Celgard 2300 film separator, and 1 M LiPF$_6$ in 1:1 ethylene carbonate (EC)/dimethyl carbonate (DMC) electrolyte. The assembly of the testing cells was carried out in an argon-filled glove box, where water and oxygen concentration were kept less than 5 ppm.

All the cells were allowed to age for 24 h before testing, specific capacity is based on the weight of nanocomposite material. Charge–discharge measurements of iron fluoride cathodes vs. Li/Li$^+$ were performed at room temperature under different rates in the voltage range of 1.0–4.5 V and 2.0–4.5 V on the Neware battery test system BTS-XWJ-6.44S-00052 (Newell, Shenzhen, China). Cyclic voltammetry (CV) tests and EIS experiments were performed on a Zahner Zennium electrochemical workstation. CV tests were carried out at a constant scanning rate of 0.2 mV s^{-1} on the potential interval 1.0–4.5 mV s^{-1} (vs. Li$^+$/Li) and 1 mV s^{-1} on the potential interval 2.0–4.5 V (vs. Li$^+$/Li), respectively. The ac perturbation signal was ±5 mV and the frequency range was from 100 mHz to 100 KHz.

3. Results and discussion

Fig. 1a shows the thermogravimetric (TG) curve of the FeF$_3$·3H$_2$O precursor obtained over the temperature range from 45 °C to 800 °C. Four distinct regions of weight-loss are found in the regions of 45–114, 114–240, 240–372, and 372–800 °C. The slight weight-loss between 45 and 114 °C can be attributed to the adsorbed water at the surface of FeF$_3$·3H$_2$O nanoparticles. A rapid weight loss (28.2%) is detected between 114 and 240 °C, which corresponds to the loss of much hydration water (2.67H$_2$O per FeF$_3$·3H$_2$O formula unit). The slight weight loss (5.1%) that occurs between 240 and 372 °C results from the complete removal of hydration water for FeF$_3$·0.33H$_2$O transforming to anhydrous FeF$_3$. There is also continuous weigh loss between 372 and 800 °C, which is probably due to the decomposition of FeF$_3$ to become FeF$_2$ at high temperature [23]. Fig. 1b shows the differential scanning calorimeter (DSC) curve of the precursor obtained over the temperature range from 25 °C to 450 °C. Two obvious decalescence peaks are located at about 110 °C and 160 °C, which can be attributed to the loss of physically absorbed water in the precursor and hydration water for FeF$_3$·3H$_2$O transforming into FeF$_3$·0.33H$_2$O, respectively. This is in accordance with the TG curve. There is no obvious decalescence peak that corresponding to the removal of hydration water of FeF$_3$·0.33H$_2$O, in that the process is a subtle and continuous transformation.

The crystal structure of as-prepared FeF$_3$·3H$_2$O, FeF$_3$·0.33H$_2$O, and FeF$_3$ has been examined by X-ray diffraction method (XRD).
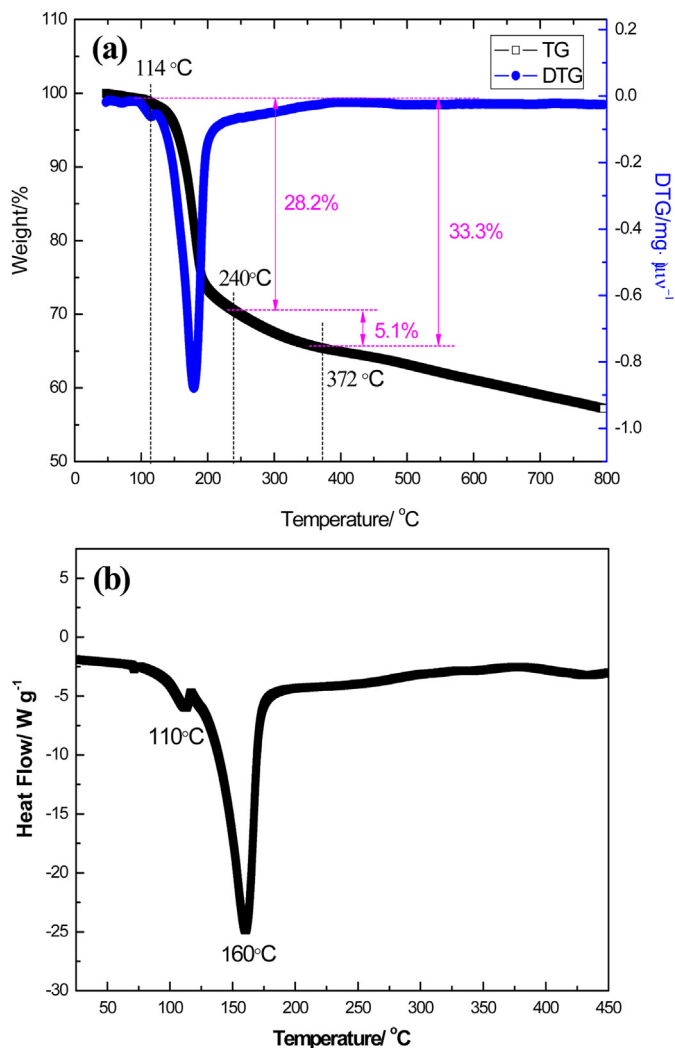
Fig. 1. TG curve of the precursor recorded from 45 °C to 800 °C (a) and DSC curve of the FeF$_3$·3H$_2$O precursor obtained over the temperature range from 25 °C to 450 °C at the heating rate of 10 °C min^{-1} in N$_2$ atmosphere (b).

From the XRD patterns and their Rietveld refinements (Fig. 2a, d and g), the three fluoride phases look quite pure. The detailed refinement parameters of these materials are listed in Table 1. The sample prepared by heat treatment at 80 °C for 10 h shows the structure of FeF$_3$·3H$_2$O (tetragonal structure with P4/n space group), the synthesized compound underwent heat treatment at 180 °C for 12 h has the structure of FeF$_3$·0.33H$_2$O (orthorhombic structure with Cmcm space group), and the sample heat-treated at 400 °C is FeF$_3$ (rhombohedral structure with R$\overline{3}$c space group). The results of XRD are in line with the results of TG and DSC (see Fig. 1). Therefore, we suggest that the following three reactions are responsible for the change of crystal structure during heat treatment:

$$Fe^{3+} + 6F^- \rightarrow FeF_6^{3-} \tag{4}$$

$$FeF_6^{3-} + 3H_2O \rightleftarrows FeF_3 \cdot 3H_2O + 3F^- \tag{5}$$

$$FeF_3 \cdot 3H_2O \rightarrow FeF_3 \cdot 0.33H_2O \rightarrow FeF_3 \tag{6}$$
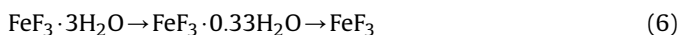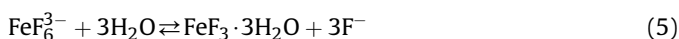
The first reaction is very favorable due to the high stability of FeF$_6^{3-}$ ($K_f = 10^{15.04}$) [24], as indicated by the rapid color change from
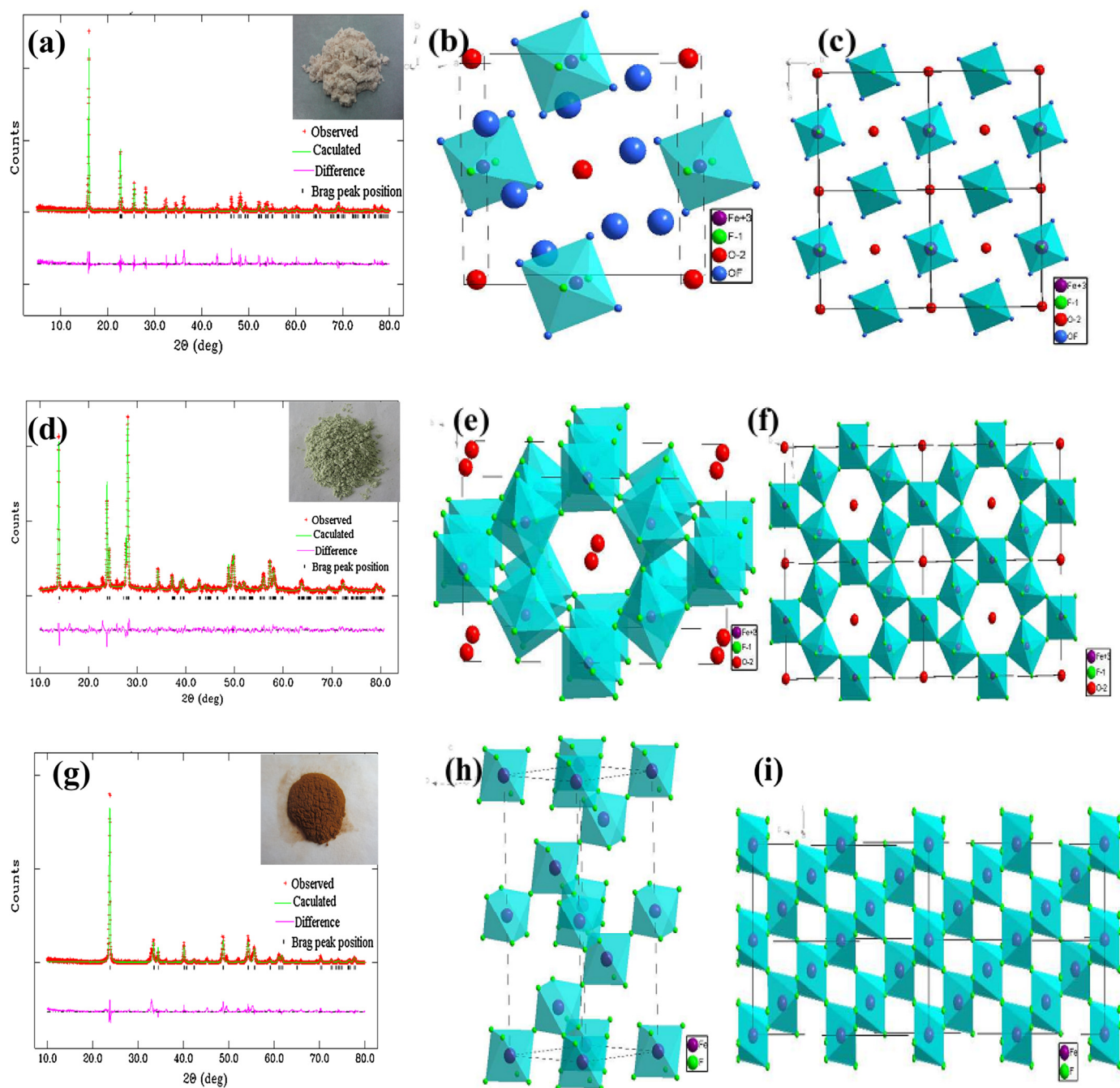
Fig. 2. XRD patterns and their Rietveld refinements of $FeF_3 \cdot 3H_2O$ (a), $FeF_3 \cdot 0.33H_2O$ (d), and FeF_3 (g). Inset: photo of the corresponding electrode powder. Unit cells for $FeF_3 \cdot 3H_2O$ (b), $FeF_3 \cdot 0.33H_2O$ (e), and FeF_3 (h). Projection of $FeF_3 \cdot 3H_2O$ along the [001] direction(c), $FeF_3 \cdot 0.33H_2O$ along the [001] direction (f), and FeF_3 along the [100] direction (i).

tawny $Fe(OH)_3$ to colorless FeF_6^{3-} by mixing the $Fe(OH)_3$ precipitation and the HF solution. As the reaction occurred in aqueous-based solution, FeF_6^{3-} readily converted to $FeF_3 \cdot 3H_2O$. The third reaction occurs when $FeF_3 \cdot 3H_2O$ is heat treated. $FeF_3 \cdot 3H_2O$ can be readily converted to $FeF_3 \cdot 0.33H_2O$ by heating in Ar atmosphere at

180 °C, and when the temperature rose up to 400 °C, $FeF_3 \cdot 3H_2O$ transforms to anhydrous FeF_3.

In order to further identify the crystal structure for these three iron fluorides ($FeF_3 \cdot 3H_2O$, $FeF_3 \cdot 0.33H_2O$, and FeF_3), the structure sketches are also shown in Fig. 2. As shown in Fig. 2b and c, each

Table 1
Lattice parameters for $FeF_3 \cdot 3H_2O$, $FeF_3 \cdot 0.33H_2O$, and FeF_3.

Samples	Space group	a (Å)	b (Å)	c (Å)	α (°)	β (°)	γ (°)	Volume (Å³)
$FeF_3 \cdot 3H_2O$	P4/n	7.831112	7.831112	3.878774	90	90	90	237.87
$FeF_3 \cdot 0.33H_2O$	Cmcm	7.380972	12.633476	7.533669	90	90	90	712.174
FeF_3	R$\bar{3}$c	5.208512	5.208512	13.334743	90	90	120	313.287

iron atom in $FeF_3 \cdot 3H_2O$ crystal structure is surrounded by six ligands in the form of a nearly regular octahedron. Adjacent octahedron shares apices of fluorine atoms to form chains along the direction of [001]. The four other ligands of each octahedron are two fluorine atoms and two water molecules statistically occupying the four positions of a square around the iron atom. It can be clearly observed that lots of vacant channels appear around the chains of $FeF_3 \cdot 3H_2O$ octahedron along the [001], which may be able to accommodate Li^+. In the structure of $FeF_3 \cdot 0.33H_2O$ (see Fig. 2e and f), six Fe octahedral are connected via corner-sharing to form a special huge hexagonal cavity, leading to a rapid pathway for Li^+ transport. As shown in Fig. 2h, the structure of FeF_3 consists of corner-sharing $FeF_{6/2}$ octahedra. All the corners of the $FeF_{6/2}$ octahedra are shared with other $FeF_{6/2}$ octahedra, forming a three-dimensional tunnel structure (see Fig. 2i). FeF_3 possesses a distorted ReO_3 structure, which is also described as an A-site deficient rhombohedral-type perovskite with $R\bar{3}c$ space group symmetry.

Though $FeF_3 \cdot nH_2O$ with different hydration water shows different structures, all these iron fluorides have good Li^+ transport channels. However, the different roles and degrees of freedom of hydration water in respective structures can significantly impact their conducting behavior and electrochemical activity. As we know, though FeF_3 has the highest theoretical specific capacity (712 mAh g^{-1}), the high ionicity of FeF_3 combined with large bandgap results in electronically insulating behavior and poor actual electrochemical performance. The existence of hydration water could improve the electronic conductivity significantly. The water molecule is immobilized inside the huge hexagonal cavity in the structure of $FeF_3 \cdot 0.33H_2O$ (see Fig. 2e and f). Besides, the water molecule can act as structural stabilizer, to stabilize the huge hexagonal cavity and avoid structure collapse during lithium ion insertion and extraction processes. However, the excess water in $FeF_3 \cdot 3H_2O$ may induce structural instability, as well as low specific capacity.

The particle size and morphology of iron fluoride compound with different crystal water observed by SEM are presented in Fig. 3. All the three samples are made of free solid crystals with the shape of bars (see Fig. 3a–f). The particles of $FeF_3 \cdot 3H_2O$ and
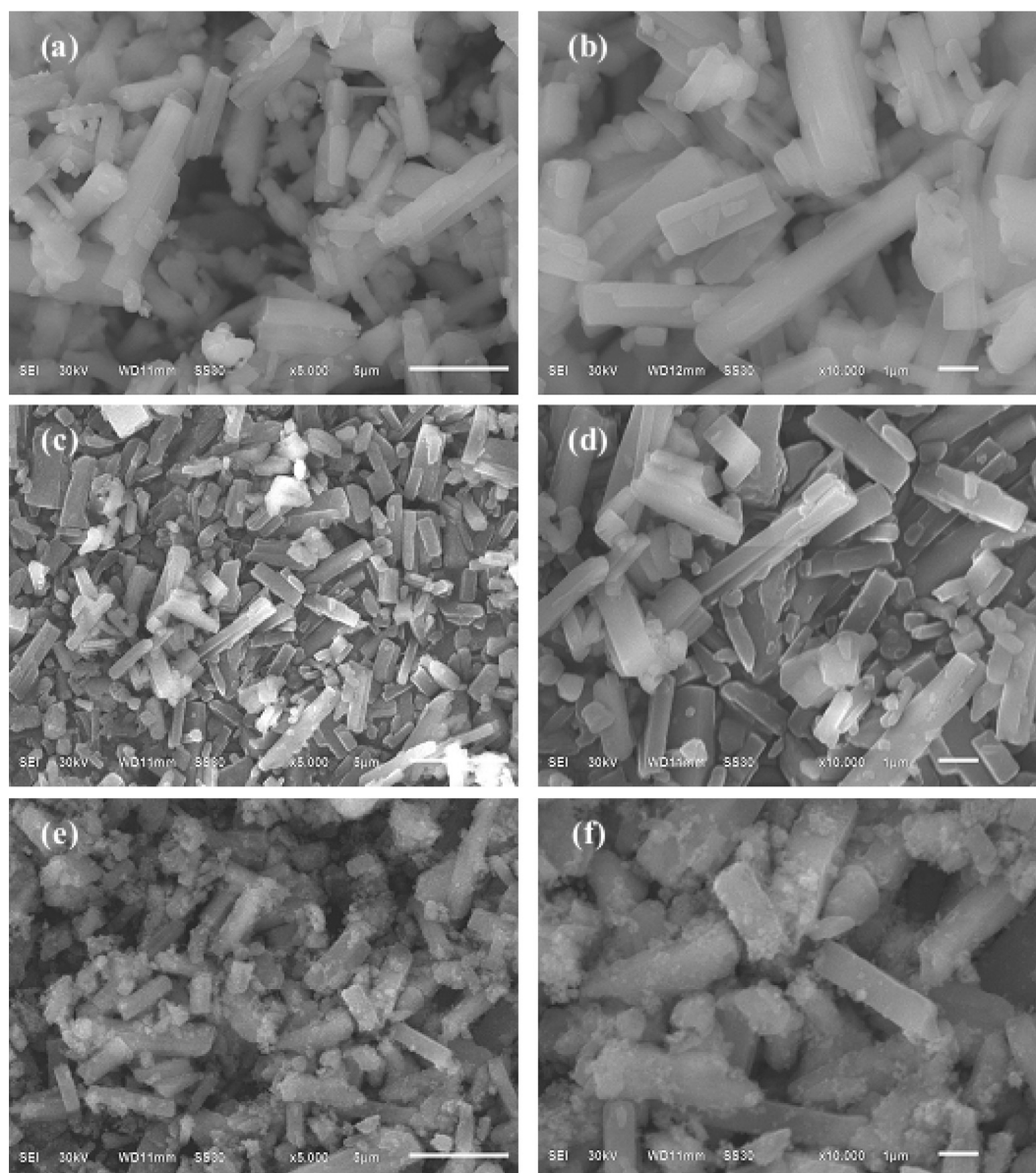

Fig. 3. SEM images of $FeF_3 \cdot 3H_2O$ (a, b), $FeF_3 \cdot 0.33H_2O$ (c, d) and anhydrous FeF_3 (e, f).

$FeF_3 \cdot 0.33H_2O$ are glossy. For $FeF_3 \cdot 3H_2O$, the shorter sides of the bars are about 1–1.5 μm, and the longer sides are up to 2–7 μm. The particle size of $FeF_3 \cdot 0.33H_2O$ is smaller than $FeF_3 \cdot 3H_2O$, its shorter sides are 0.3–0.9 μm, and longer sides are 0.5–4.5 μm, which can be attributed to the dehydration after heat treatment. Fig. 3e and f shows obvious difference of morphology for anhydrous FeF_3, the particles become irregular and rough, some tiny particles are dispersed on the surface of bar-like particles and agglomerate together, this is may be due to the small bar shape of particles have been changed to granule under high temperature.

Fig. 4 shows the discharge and charge profiles of $FeF_3 \cdot 3H_2O$, $FeF_3 \cdot 0.33H_2O$, and FeF_3 at a constant current density of 0.5 C (1 C = 237 mA g^{-1}) in the voltage range of 2.0–4.5 V. All of these samples show low specific capacity, which is probably caused by their poor electronic conductivity. FeF_3 delivers the lowest initial discharge capacity of 30.5 mAh g^{-1}. $FeF_3 \cdot 3H_2O$ also delivers low initial discharge capacity (48.4 mAh g^{-1}). Obviously, $FeF_3 \cdot 0.33H_2O$ shows the highest discharge capacity of 88.0 mAh g^{-1}. After 50 cycles, the discharge capacities of $FeF_3 \cdot 3H_2O$, $FeF_3 \cdot 0.33H_2O$, and FeF_3 decrease to 26.0, 55.9, and 26.4 mAh g^{-1}, respectively. $FeF_3 \cdot 0.33H_2O$ shows much better electrochemical performance than $FeF_3 \cdot 3H_2O$ and FeF_3, which may be due to its special structure (the huge hexagonal cavity for Li^+ transfer). Besides, the potential difference between discharge profile and corresponding charge profiles of $FeF_3 \cdot 0.33H_2O$ cathode is smaller than those of $FeF_3 \cdot 3H_2O$ and FeF_3, indicating it has the smallest electrochemical polarization. Although orthorhombic $FeF_3 \cdot 0.33H_2O$ exhibits the best electrochemical activity among these three samples, the specific capacity is much lower than theoretical capacity and the cycle stability is very poor. Ball milling with conductive agent to form composites is a simple and efficient method to improve the electronic conductivity of electrode materials. To further improve their electrochemical properties, a ball milling process with acetylene
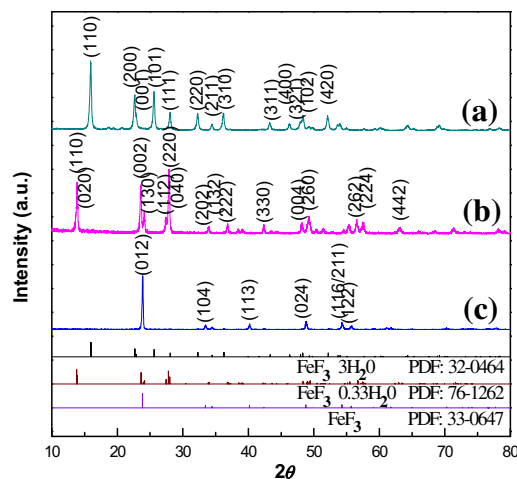

Fig. 5. XRD patterns of $FeF_3 \cdot 3H_2O/C$ (a), $FeF_3 \cdot 0.33H_2O/C$ (b), and FeF_3/C nanocomposite (c).

black (AB) has been used to form $FeF_3 \cdot 3H_2O/C$, $FeF_3 \cdot 0.33H_2O/C$, and FeF_3/C nanocomposites.

The XRD patterns of $FeF_3 \cdot 3H_2O/C$, $FeF_3 \cdot 0.33H_2O/C$ and FeF_3/C samples are presented in Fig. 5. It can be seen that the diffraction patterns of all samples are consistent with the corresponding standard $FeF_3 \cdot 3H_2O$ (JCPDS card no. 32-0464), $FeF_3 \cdot 0.33H_2O$ (JCPDS card no.76-1262), and FeF_3 (JCPDS card no. 33-0647) with no carbon signals are detected, which is due to the AB is amorphous.

Fig. 6 shows the SEM images of the $FeF_3 \cdot 3H_2O/C$, $FeF_3 \cdot 0.33H_2O/C$, and FeF_3/C nanocomposites. After ball-milling with AB for 3 h, the particle diameter was reduced greatly. All the three composites are made of agglomerated particles with no visible crystal shape,
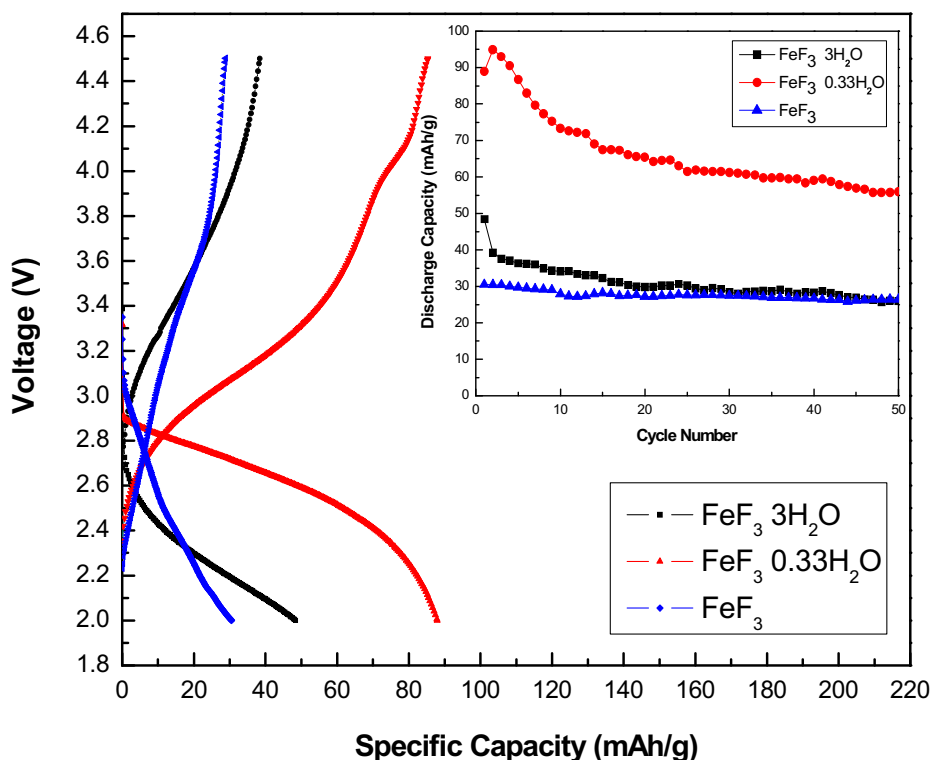

Fig. 4. Discharge and charge profiles of $FeF_3 \cdot 3H_2O$, $FeF_3 \cdot 0.33H_2O$, and anhydrous FeF_3 at 0.5 °C. Inset: cycling stability curves of $FeF_3 \cdot 3H_2O$, $FeF_3 \cdot 0.33H_2O$, and FeF_3 at 0.5 °C in the voltage of 2.0–4.5 V.
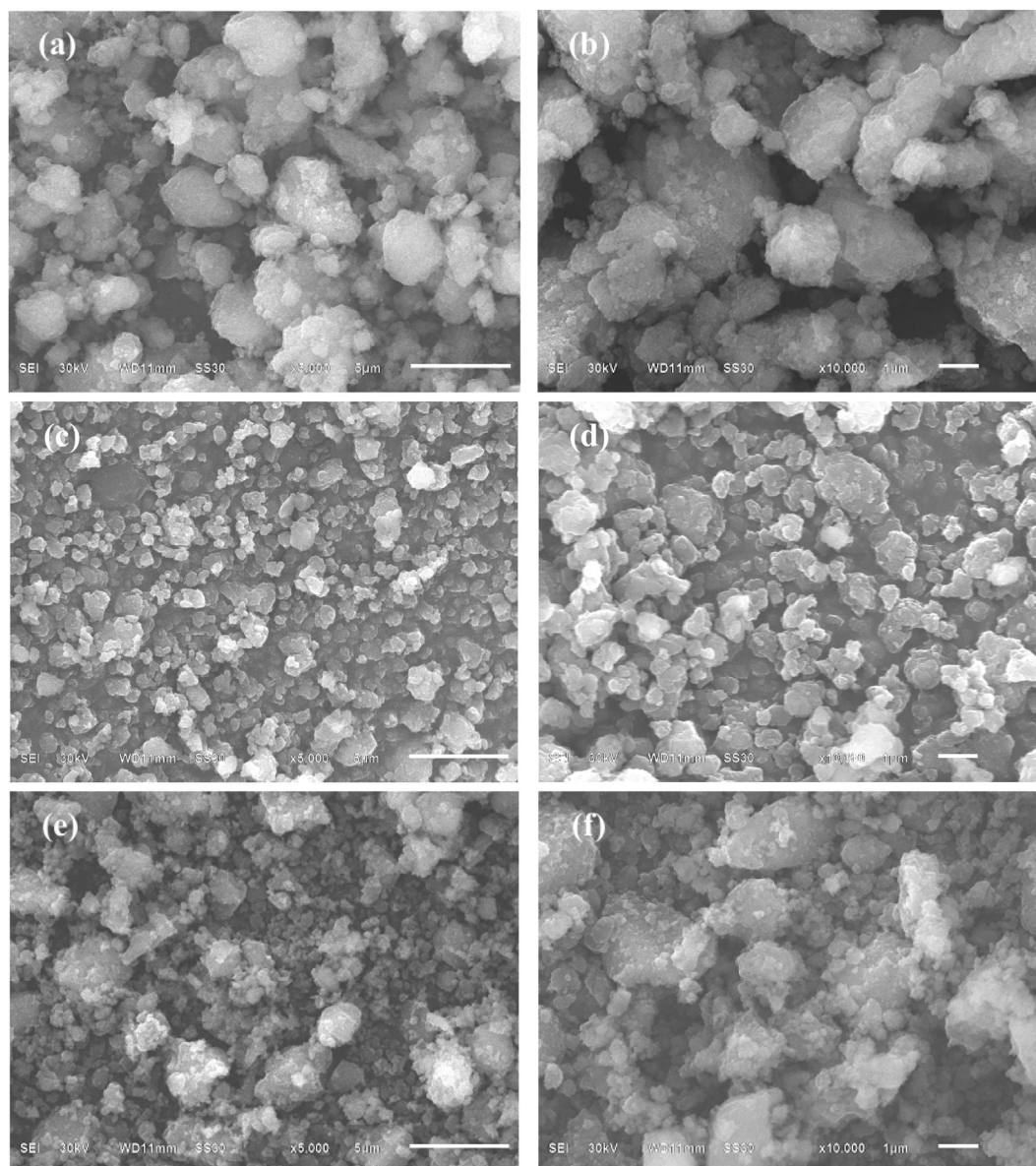
Fig. 6. SEM images of FeF$_3$·3H$_2$O/C (a, b), FeF$_3$·0.33H$_2$O/C (c, d), and FeF$_3$/C nanocomposites (e, f).

which are composed of many fine particles (ee Fig. 6a–f). FeF$_3$·3H$_2$O/C material turned humid and closely packed together due to existence of excess hydration water, so the particle size of FeF$_3$·3H$_2$O/C is larger than the other two samples with a broad particle size distribution of 0.2–3.5 μm. The particle size of FeF$_3$/C is about 0.1–2.6 μm as the tiny particles aggregate severely during high temperature processing in Ar. Appropriate heat treatment can reduce the particle size and particles agglomeration, thus narrowing the particle size distribution. Therefore, FeF$_3$·0.33H$_2$O/C composite has the most even particle distribution diameter with a particle size of 0.1–1.7 μm.

The micromorphology of iron fluoride-C nanocomposites can be observed more clearly by TEM (transmission electron microscopy) images. Fig. 7a, c and e is TEM images of FeF$_3$·3H$_2$O/C, FeF$_3$·0.33H$_2$O/C, and FeF$_3$/C, respectively. No obvious distinction can be observed among these nanocomposites. Each of them is large clusters, which are made of many smaller particles. As depicted in Fig. 7b, d and f, HRTEM (high-resolution transmission electron microscopy) images show that these nanocomposites are

of nanocrystalline regions encapsulated by an amorphous carbon matrix, which indicates that iron fluoride materials and acetylene black powders were mixed uniformly and closely interlinked with each other after ball-milling. However, the grain size is different. Fig. 7b reveals FeF$_3$·3H$_2$O nanocrystalline is about 6–13 nm in diameter, Fig. 7d reveals FeF$_3$·0.33H$_2$O nanocrystalline is about 2–7 nm in diameter, while FeF$_3$/C nanocrystalline is about 5–10 nm in diameter (Fig. 7f). The selective area electron diffraction (SAED) patterns of three iron fluoride composites can be observed in Fig. 7g–i, which conform the distinct crystal symmetry. Fig. 7g shows two ring patterns related to (110), (200) planes, and the indices correspond to tetragonal FeF$_3$·3H$_2$O. Fig. 7h shows two ring patterns related to (110), (002) planes which corresponding to orthorhombic FeF$_3$·0.33H$_2$O. Fig. 7i shows two ring patterns related to (012), (024) planes, and the indices correspond to rhombohedral FeF$_3$. This data are in line with the XRD results shown in Fig. 5. The AB particles in the iron fluoride-C nanocomposites contribute to the form of network, which can interconnect the isolated particles, so that the electrons can be readily transmitted to the sites where
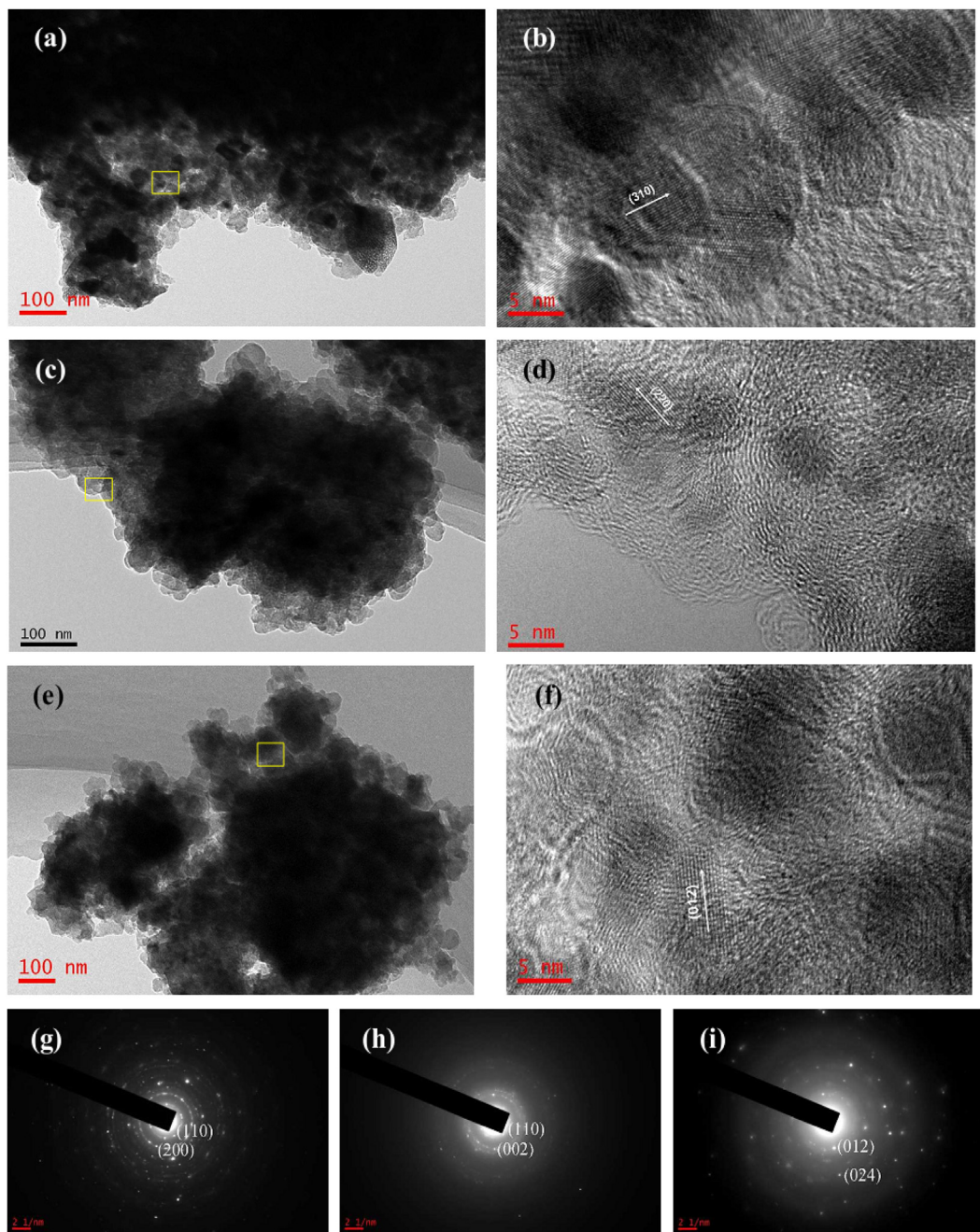
Fig. 7. TEM images of FeF$_3$·3H$_2$O/C (a), FeF$_3$·0.33H$_2$O/C (c), and FeF$_3$/C nanocomposites (e); HRTEM images of FeF$_3$·3H$_2$O/C (b), FeF$_3$·0.33H$_2$O/C (d), and FeF$_3$/C (f); SAED patterns of FeF$_3$·3H$_2$O/C (g), FeF$_3$·0.33H$_2$O/C (h), and FeF$_3$/C (i).

redox reactions take place. Moreover, smaller particles will induce shorter diffusion distance of Li$^+$, FeF$_3$·0.33H$_2$O/C has the smallest and most even particle size, and good network structure, which is considered to be beneficial to electrolyte infiltration and electrochemical reactivity. For these reasons, iron fluorides after ball-milling with AB will show better electrochemical performance as shown and discussed in the following section.

Although the electrochemical reaction mechanism of FeF$_3$ has been investigated fully, the electrochemical reaction mechanisms of FeF$_3$·0.33H$_2$O and FeF$_3$·3H$_2$O still remains unknown. To explore the reaction mechanisms of these three iron fluorides and compare their electrochemical properties, the galvanostatic charge–discharge measurements are carried out between a wide voltage range (1.0–4.5 V). Fig. 8a–c shows the discharge and charge profiles of FeF$_3$·3H$_2$O/C, FeF$_3$·0.33H$_2$O/C and FeF$_3$/C as cathodes during the first 5 cycles with a current density of 0.1 C in the voltage of 1.0–4.5 V at room temperature. Herein, the capacity is calculated on the composite materials. Obviously, two voltage plateaus in discharge process and corresponding charge plateaus can be detected clearly in all three samples. The FeF$_3$·0.33H$_2$O/C nanocomposites showed a well-defined two-staged discharge with a higher voltage plateau above 2.0 V, followed with a flat voltage discharge at 2.0–1.0 V, demonstrating a two-step electrochemical reaction process. FeF$_3$·3H$_2$O/C and FeF$_3$/C show similar discharge plateaus. These discharge features in Fig. 8a–c are very similar to those observed from the ball-milled FeF$_3$/C samples at small current density
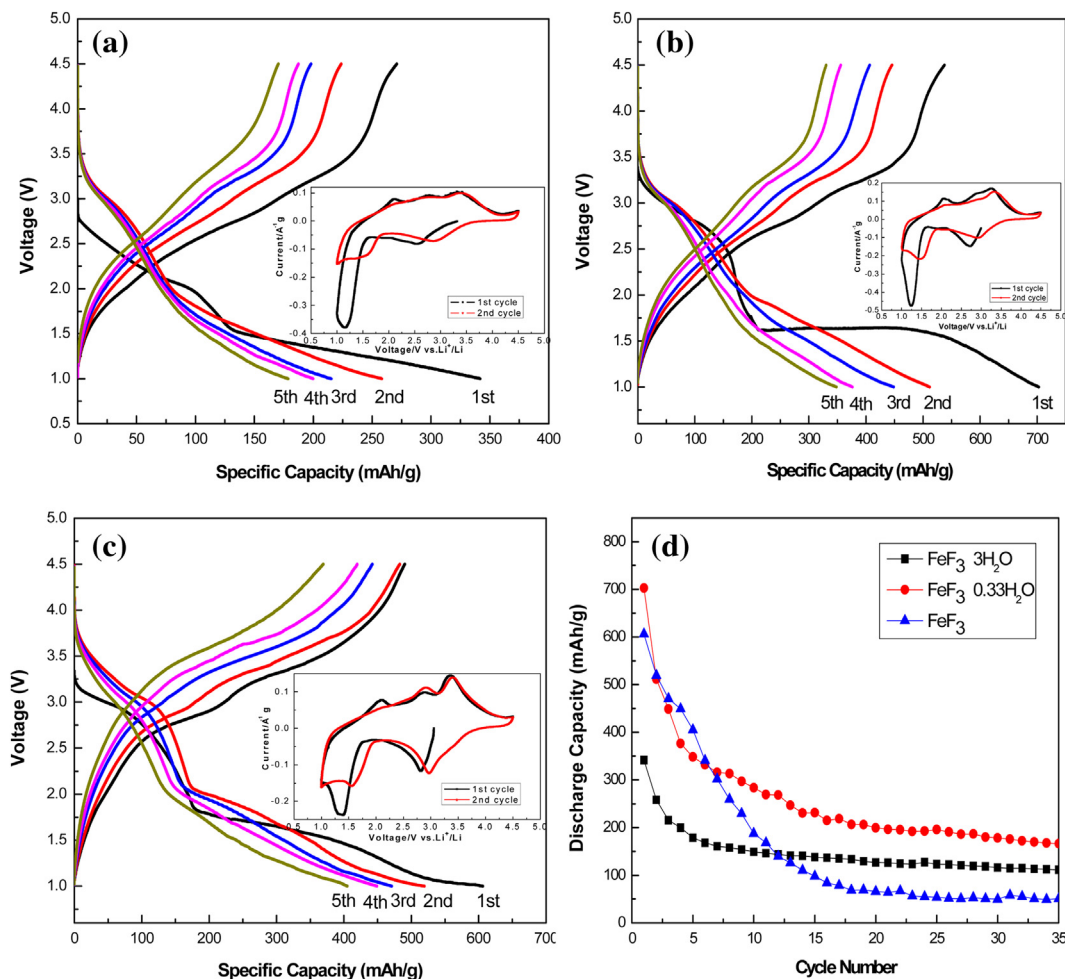
Fig. 8. Discharge and charge profiles of $FeF_3 \cdot 3H_2O/C$ (a), $FeF_3 \cdot 0.33H_2O/C$ (b), and FeF_3/C composite (c) during the first 5 cycles at 0.1 °C in the voltage of 1.0–4.5 V. Insets: respective CV curves during the first two cycles at a scan rate of 0.2 mV s^{-1}. Cycling stability curves of three iron fluoride composites at 0.1 °C in the voltage of 1.0–4.5 V (d).

[8,25,26], which are probably attributed to a two-step electrochemical reaction including Li$^+$ insertion and reversible conversion reaction. Notably, $FeF_3 \cdot 0.33H_2O/C$ shows maximum initial discharge capacity of 702.9 mAh g^{-1}. In comparison, $FeF_3 \cdot 3H_2O/C$ and FeF_3/C deliver initial discharge capacities of 341.7 and 606.0 mAh g^{-1} at first cycle, respectively. After 5 cycles, the discharge capacities of $FeF_3 \cdot 3H_2O/C$, $FeF_3 \cdot 0.33H_2O/C$ and FeF_3/C are 178.7, 348.2 and 404 mAh g^{-1}, respectively. Though FeF_3/C electrode has the best capacity retention during the first 5 cycles, its capacity reduces sharply after 10 cycles, as described in Fig. 8d. The discharge capacity of $FeF_3 \cdot 3H_2O/C$, $FeF_3 \cdot 0.33H_2O/C$, and FeF_3/C after 35 cycles is 111.4, 166.5, 50.5 mAh g^{-1} and the capacity retentions are 32.6%, 23.7%, 8.33%, respectively. The low capacity retention of FeF_3/C totally indicates the decrease of kinetics in conversion reaction during cycling. It is worth noting that though $FeF_3 \cdot 3H_2O/C$ nanocomposite shows the highest capacity retention, its specific capacity is much smaller compared with $FeF_3 \cdot 0.33H_2O/C$. To sum up, $FeF_3 \cdot 0.33H_2O/C$ has the best electrochemical performance, which ascribes its special structure with huge hexagonal cavity and uniform particles. Certainly, the cycle performance of $FeF_3 \cdot 0.33H_2O/C$ is also unsatisfied during the voltage of 1.0–4.5 V.

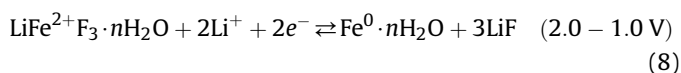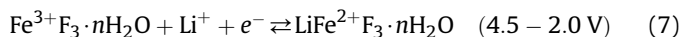To further investigate the electrochemical behaviors of $FeF_3 \cdot 3H_2O/C$, $FeF_3 \cdot 0.33H_2O/C$ and FeF_3/C composites, the cyclic voltammograms (CV) of these three nanocomposites were measured at a scan rate of 0.2 mV s^{-1} in the voltage of 1.0–4.5 V as shown in the insets of Fig. 8. All samples have the similar oxidation/

reduction peaks, suggesting that these samples have similar electrochemical reaction mechanism. In the first cycle, there is a reduction peak at about 2.8 V for all three nanocomposites, which may be due to the Li$^+$ insertion process. Meanwhile, there is a big reduction peak in the range of 1.0–1.5 V, which can be attributed to the reversible conversion reaction. These are in accordance with the discharge profiles at the first cycle, corresponding to Li$^+$ insertion into the $FeF_3 \cdot nH_2O$ ($n = 0, 0.33, 3$) to form $LiFe^{2+}F_3 \cdot nH_2O$ and successive reductive decomposition of $LiFe^{2+}F_3 \cdot nH_2O$ into LiF and Fe^0. In reversed scan, the oxidation peak at 2.0 V relates to the conversion reaction of LiF–Fe^0 to form $LiFe^{2+}F_3 \cdot nH_2O$ phase, and the oxidation peak in the range of 3.0–3.5 V is due to the $LiFe^{2+}F_3 \cdot nH_2O$ phase to regenerate $FeF_3 \cdot nH_2O$ nanocrystals. The electrochemical behavior of FeF_3/C conforms to the previous reports. However, what appears to be interesting is that both of $FeF_3 \cdot 0.33H_2O/C$ and $FeF_3 \cdot 3H_2O/C$ also have the similar electrochemical behaviors as FeF_3/C, which has not been identified before. This will be further proved by the following XRD tests. Besides, it should be noted that the intensity of reduction peaks of these three nanocomposites at lower voltage decreases sharply and the corresponding oxidation peaks (at about 2.0 V) are unobvious at the second cycle. However, the redox peaks at higher voltage maintain relatively identical intensity with the first cycle. So the reversible conversion reaction process for these iron fluorides shows poor reversibility, while the Li$^+$ insertion/extraction process shows relatively good reversibility. It is possible to improve the

cycle performance of these iron fluorides remarkably by controlling the discharge and charge voltage in the range of 2.0–4.5 V, only for Li^+ insertion/extraction.

In order to understand the discharge–charge processes and further confirm the CV features and related structural conversions, we also performed XRD analysis of $FeF_3 \cdot 3H_2O/C$, $FeF_3 \cdot 0.33H_2O/C$ and FeF_3/C electrodes in different discharge–charge states at first cycle at 0.1 C in the voltage of 1.0–4.5 V. The powder was removed from aluminum foil in an Ar-filled glove box, washed by dimethyl carbonate (DMC), and then it was dried and kept in a sealed glass phial to minimize atmospheric exposure until analyzed. As shown in Fig. 9, when the electrode discharging to 2.0 V, typical diffraction peaks of $FeF_3 \cdot 3H_2O/C$, $FeF_3 \cdot 0.33H_2O/C$ and FeF_3/C are well maintained, and no other signal associated with newly generated phases emerges. This confirms the solid-solution behavior and structural stability during the Li^+ insertion process above 2.0 V. When discharging to 1.5 V, the characteristic peaks of these three iron fluoride materials are no longer visible. Instead, a group of new peaks at 38.7, 45.0, 65.5, 44.6, and 65° appear, which can be well-indexed to LiF (JCPDS no.78-1217) and Fe^0 (JCPDS no.06-0696), indicating the conversion reaction of Fe^{2+} to Fe^0 happens. When the electrode is fully discharged to 1.0 V, the XRD signals of LiF and Fe^0 become stronger. The fully lithiated sample consists of Fe^0 and LiF as described previously [13].

In reversed charge process, the diffraction peaks of $FeF_3 \cdot 3H_2O/C$, $FeF_3 \cdot 0.33H_2O/C$ and FeF_3/C phases reappear and become intense again and the original two-theta positions are restored as the fresh materials when recharging to 4.5 V. This reversible change in XRD patterns evidently demonstrates the reversible structure of three ion fluoride electrodes. Consequently, $FeF_3 \cdot 3H_2O$, $FeF_3 \cdot 0.33H_2O$ and FeF_3 have the identical mechanism of reversible electrochemical reaction. Therefore, the discharge process of $FeF_3 \cdot nH_2O$ ($n = 0, 0.33, 3$) can be described in the following reactions:

$$Fe^{3+}F_3 \cdot nH_2O + Li^+ + e^- \rightleftarrows LiFe^{2+}F_3 \cdot nH_2O \quad (4.5-2.0\,V) \quad (7)$$

$$LiFe^{2+}F_3 \cdot nH_2O + 2Li^+ + 2e^- \rightleftarrows Fe^0 \cdot nH_2O + 3LiF \quad (2.0-1.0\,V) \quad (8)$$

Reaction (7) is an intercalation reaction, corresponding to the insertion/extraction of Li^+ into $FeF_3 \cdot nH_2O$ lattice in the voltage range of 4.5–2.0 V. The original structure of $FeF_3 \cdot nH_2O$ is maintained in this reaction with a slight lattice change provoked by the Li^+ insertion. Reaction (8) is a conversion reaction, which involves a complete structural reconstruction in the voltage range of 2.0–1.0 V and the original structure of $LiFeF_3 \cdot nH_2O$ is fully destroyed to form LiF–Fe·nH_2O nanocrystals.

During the repetitive conversion reaction, enormous stress in crystal lattice would occur at different discharge–charge states, and the resulting structure would be randomized, displaying exceptionally broadened diffraction peaks. Furthermore, the by-product of LiF would increase the electrode resistance for its insulating property [27]. These complications are associated with the poor cycling performance in the voltage range of 1.0–4.5 V (see Fig. 8). For this reason, the electrochemical behaviors tested in a limited voltage range of 2.0–4.5 V to prevent the conversion reaction are shown in Fig. 10. It is obvious that the cycle performance of these three iron fluorides is improved significantly by increasing the cut-off voltage to 2.0 V. Rate performance is crucial in view of the suitability of fluoride cathodes applied in high-power lithium batteries. In order to demonstrate the impact of crystal water, the initial discharge/charge profiles of $FeF_3 \cdot 3H_2O/C$, $FeF_3 \cdot 0.33H_2O/C$, and FeF_3/C at different rates (0.1–5 C) in the voltage range of 2.0–4.5 V at room temperature are shown in Fig. 10a, c and e. The initial
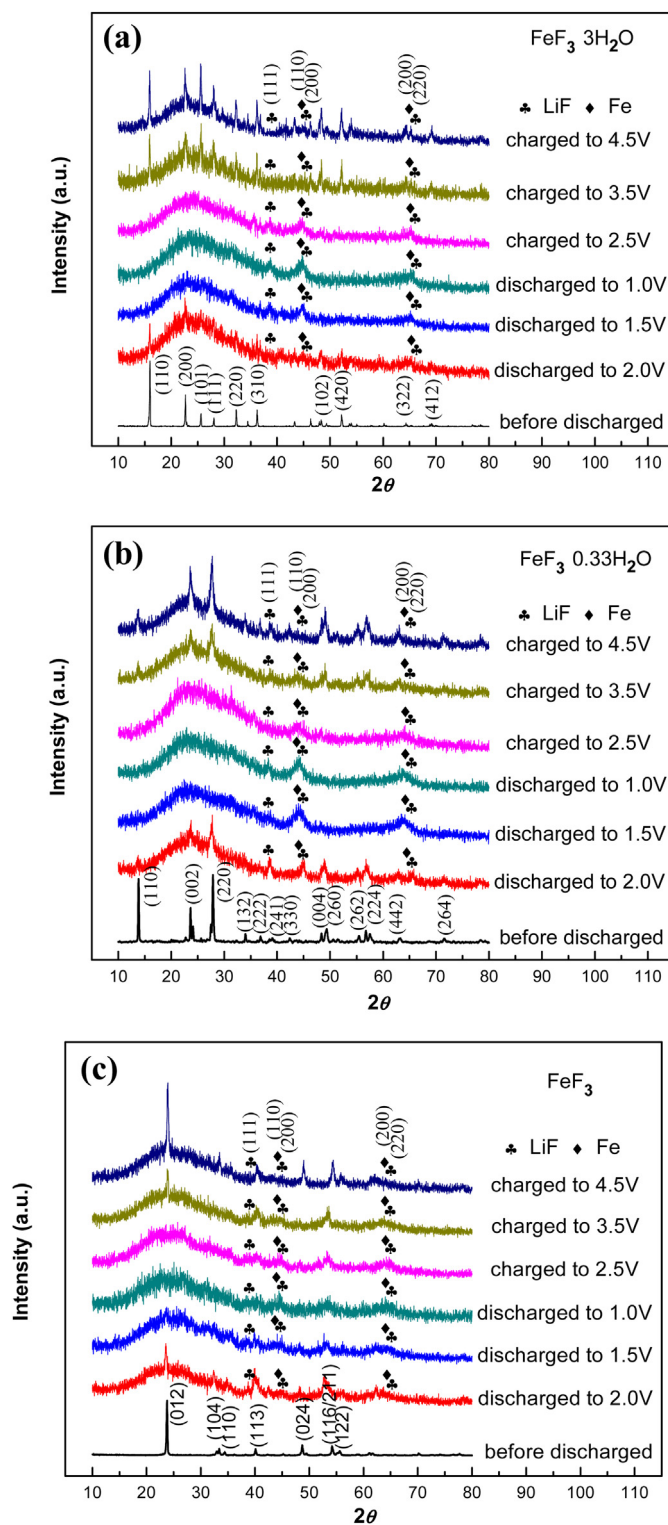

Fig. 9. XRD patterns of the $FeF_3 \cdot 3H_2O/C$ (a), $FeF_3 \cdot 0.33H_2O/C$ (b) and FeF_3/C (c) electrodes at different discharge and charge states of the first cycle at a current density of 0.1 C in the voltage of 1.0–4.5 V.

discharge capacities of $FeF_3 \cdot 3H_2O/C$, $FeF_3 \cdot 0.33H_2O/C$, and FeF_3/C are 92.8, 177.6, and 167.9 mAh g^{-1} at 0.1 C, respectively. What is more interesting is that the high capacity is still sustained even at high current rates for $FeF_3 \cdot 0.33H_2O/C$ electrode. At high rates of 1 C, 2 C and 5 C, $FeF_3 \cdot 0.33H_2O/C$ exhibits reversible capacities as high as 130.2, 120.2, and 105.1 mAh g^{-1}, respectively, without serious
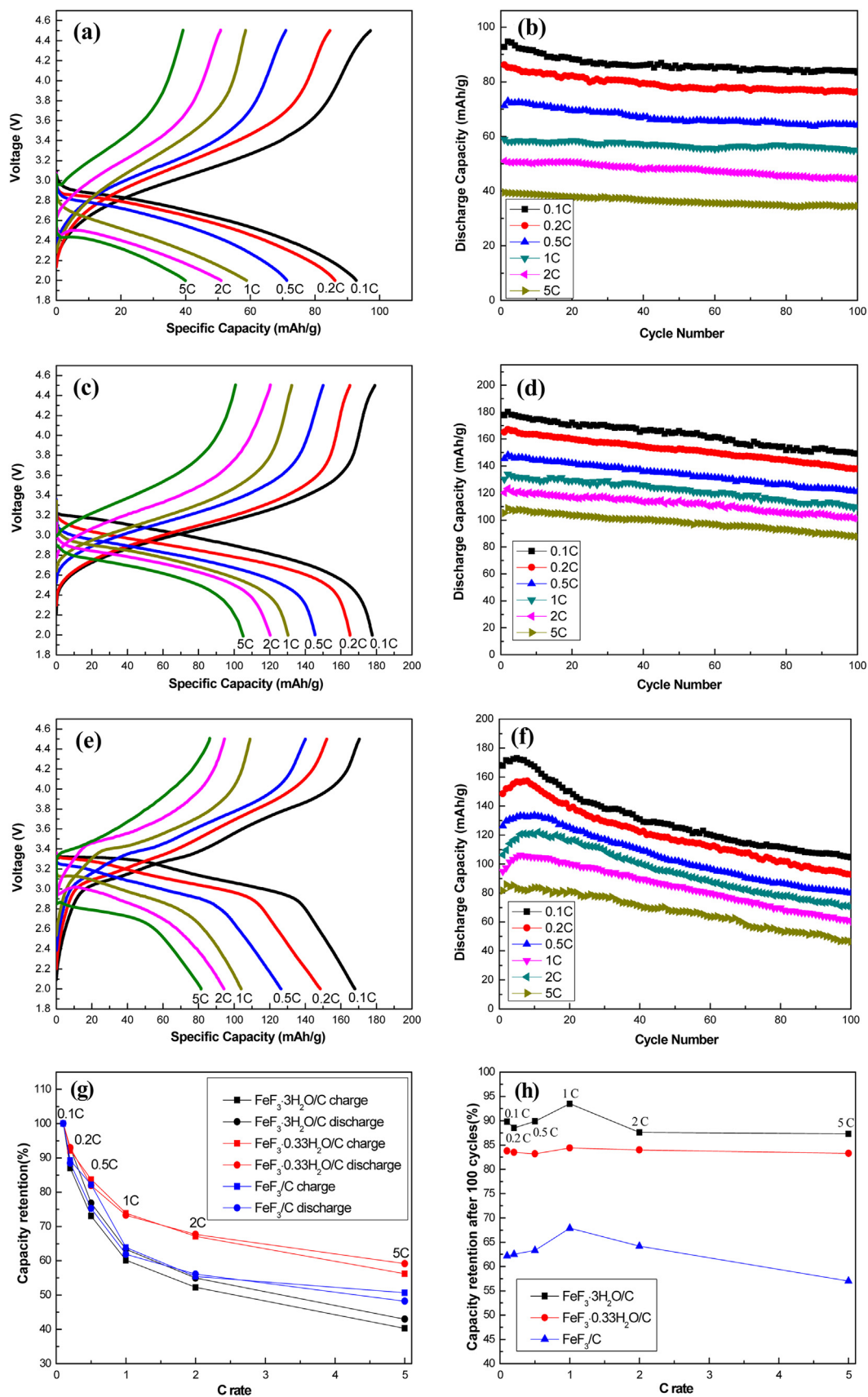
Fig. 10. Initial discharge and charge profiles of FeF$_3$·3H$_2$O/C (a), FeF$_3$·0.33H$_2$O/C (c), and FeF$_3$/C nanocomposite (e). Cycling stability curves of FeF$_3$·3H$_2$O/C (b), FeF$_3$·0.33H$_2$O/C (d), and FeF$_3$/C (f) at different rates in the voltage of 2.0−4.5 V. Capacity remaining ratios of FeF$_3$·3H$_2$O/C, FeF$_3$·0.33H$_2$O/C, and FeF$_3$/C under high C rates as compared to the capacity under 0.1 °C (g). Capacity remaining ratios of FeF$_3$·3H$_2$O/C, FeF$_3$·0.33H$_2$O/C, and FeF$_3$/C after 100 cycles under different C rates (h).

polarization degradation. The capacity retention ratios of $FeF_3 \cdot 0.33H_2O/C$ under high C rates as compared to the capacity under 0.1 C are much higher than those of $FeF_3 \cdot 3H_2O/C$ and FeF_3/C (see Fig. 10g), indicating the best rate performance of $FeF_3 \cdot 0.33H_2O/C$.

The cycle performance at different rates of $FeF_3 \cdot 3H_2O/C$, $FeF_3 \cdot 0.33H_2O/C$, and FeF_3/C nanocomposites are shown in Fig. 10b, d and f. $FeF_3 \cdot 0.33H_2O/C$ shows much better cyclic performance than FeF_3/C (see Fig. 10h). The discharge capacities of $FeF_3 \cdot 0.33H_2O/C$ after 100 cycles at 0.1, 0.2, 0.5, 1.0 and 2.0 C are 148.9, 137.9, 121.0, 109.9 and 101.0 mAh g^{-1}, respectively. Even at a high rate of 5 C, the discharge capacity of the $FeF_3 \cdot 0.33H_2O/C$ composite is 87.6 mAh g^{-1} after 100 cycles, retaining approximately 83.3% of the initial capacity. However, FeF_3/C suffers from severe capacity fading and has a discharge capacity of only 46.4 mAh g^{-1} after 100 cycles, retaining approximately 57% of the initial capacity. The data demonstrate the excellent capacity retention of the $FeF_3 \cdot 0.33H_2O/C$ nanocomposite at different rates. Surprisingly, $FeF_3 \cdot 3H_2O/C$ even shows better cycle performance than $FeF_3 \cdot 0.33H_2O/C$, which is likely to be ascribed to the less freedom of corner-coordinated hydration water molecules. It is worth noting that though $FeF_3 \cdot 3H_2O/C$ composite shows the highest capacity retention, its
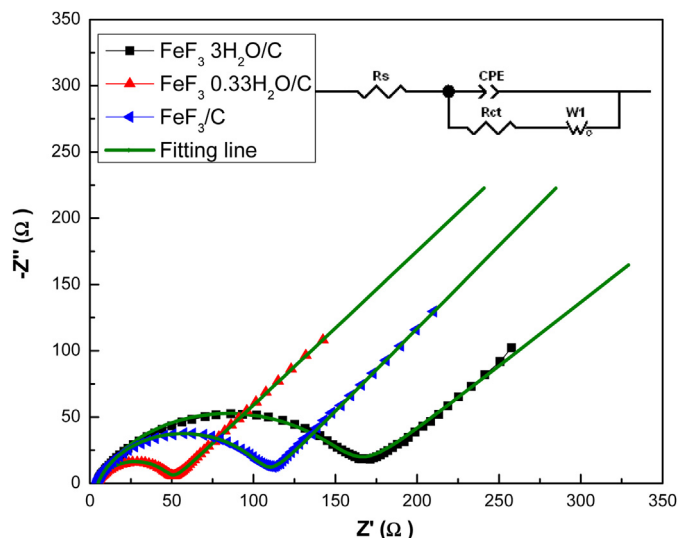

Fig. 12. Nyquist plots measured for $FeF_3 \cdot 3H_2O$, $FeF_3 \cdot 0.33H_2O/C$, and FeF_3/C composite. (Inset: the simplified equivalent circuit model).

specific capacity is much smaller compared with $FeF_3 \cdot 0.33H_2O/C$. Noticeably, capacity fading is some what more pronounced at lower rates, especially for $FeF_3 \cdot 3H_2O/C$ composite. The increased capacity fading at low rate is a common phenomenon in nanometric cathode materials and probably resulting from a combination of increased reactivity toward the electrolyte and prolonged contact between the active material and electrolyte. In any case, $FeF_3 \cdot 0.33H_2O/C$ exhibits the best electrochemical properties over a wide range of rate capabilities in the voltage of 2.0–4.5 V for traditional insertion and extraction reaction. It has been demonstrated that both lithium ion diffusion and electronic conduction play critical roles in the electrochemical properties of electrode materials. The uniformly distributed carbon particles formed a good network of electrically conductive paths among the $FeF_3 \cdot 0.33H_2O$ particles, which are closely interlinked with each other. So the active $FeF_3 \cdot 0.33H_2O$ material can be fully utilized for lithium insertion and extraction reactions. Moreover, the special huge hexagonal cavity provides the wide and stable lithium ion diffusion tunnels for $FeF_3 \cdot 0.33H_2O$.

Fig. 11a compares the cyclic voltammograms (CV) curves of $FeF_3 \cdot 3H_2O/C$, $FeF_3 \cdot 0.33H_2O/C$, and FeF_3/C composite at a scan rate of 1 mV s^{-1} in the voltage of 2.0–4.5 V. A pair of redox peaks is observed for three samples, suggesting that these three samples have the similar insertion and extraction reaction mechanism between 2.0 and 4.5 V. This is in accordance with the results of Fig. 10. The oxidation and reduction peaks are centered at 3.35 and 2.38 V for $FeF_3 \cdot 3H_2O/C$. The potential interval (ΔE) is found to be 0.97 V, indicating a serious polarization behavior. The redox peaks of FeF_3/C are located at 3.52 and 2.79 V, and the ΔE is 0.73 V. However, the redox peaks of $FeF_3 \cdot 0.33H_2O/C$ are located at 3.31 and 2.72 V, and the ΔE is only 0.59 V, which is the smallest among these three fluoride materials, showing small polarization and good reversibility. This is consistent with the outstanding rate capability and

Fig. 11. CV curves of $FeF_3 \cdot 3H_2O/C$, $FeF_3 \cdot 0.33H_2O/C$, and FeF_3/C composite at a scan rate of 1 mV s^{-1} (a); CV curves of $FeF_3 \cdot 0.33H_2O/C$ composite during first 50 cycles at a scan rate of 4 mV s^{-1} (b) in the voltage of 2.0–4.5 V.

Table 2
EIS parameters for $FeF_3 \cdot 3H_2O/C$, $FeF_3 \cdot 0.33H_2O/C$, and FeF_3/C composite.

Samples	R_s (Ω)	R_{ct} (Ω)
$FeF_3 \cdot 3H_2O/C$	4.954	155.9
$FeF_3 \cdot 0.33H_2O/C$	4.268	44.99
FeF_3/C	4.635	102.5
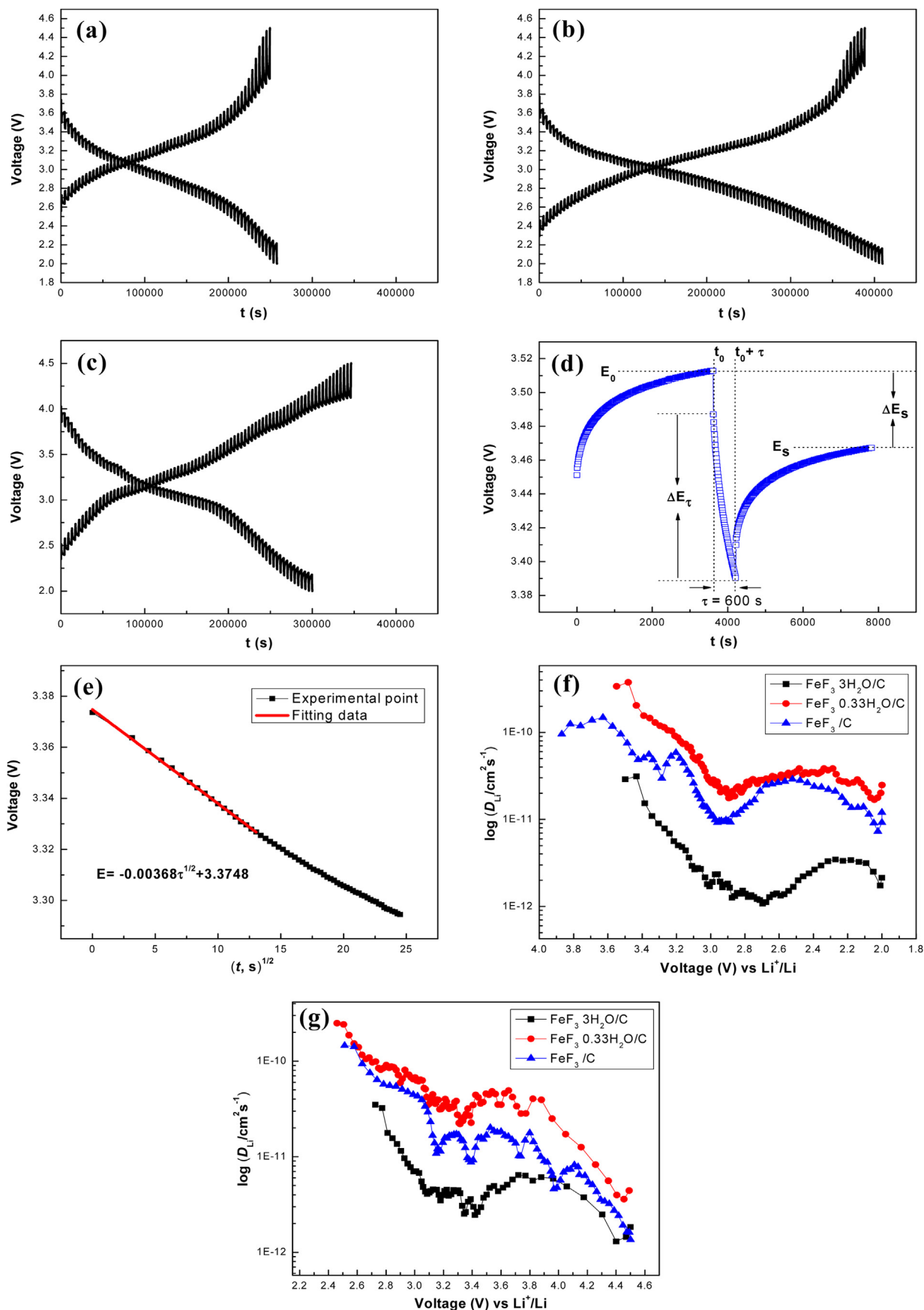
Fig. 13. The discharge/charge GITT curves of FeF$_3$·3H$_2$O/C (a) FeF$_3$·0.33H$_2$O/C electrode (b) and FeF$_3$/C (c) as a function of time in the potential range of 2.0–4.5 V. E vs. t profile of FeF$_3$ electrode for a single GITT during discharge process at 3.46 V with schematic representation of different profile parameters (d). Linear behavior of the transient voltage changes (E) vs. ($\tau^{1/2}$) during a single titration process (e). The calculated D_{Li} from the GITT data as a function of potential during discharge process (e) and charge process (f) for FeF$_3$·3H$_2$O/C, FeF$_3$·0.33H$_2$O/C, and FeF$_3$/C composite.

cycle performance of the FeF$_3$·0.33H$_2$O/C composite. Moreover, the CV profile of FeF$_3$·0.33H$_2$O/C composite exhibits the highest peak current, which facilitates the kinetic process of the electrochemical reactions, indicating the highest specific capacity. The CV curves of FeF$_3$·0.33H$_2$O/C nanocomposite during the first 50 cycles at a constant scanning rate of 4 mV s^{-1} are shown in Fig. 11b. With the cycle number increasing, the peak current densities change little and the CV curves are nearly identical, indicating the FeF$_3$·0.33H$_2$O/C nanocomposite shows excellent cycle performance. This is in accordance with the long-term cycling stability of FeF$_3$·0.33H$_2$O/C as shown in Fig. 10d. In conclusion, as compared with FeF$_3$·3H$_2$O/C and FeF$_3$/C, FeF$_3$·0.33H$_2$O/C nanocomposite has more intense cathodic and anodic peaks, less polarization (lowest ΔE), indicating a prominent specific capacity, cycle performance, and rate capability.

The Nyquist plots of FeF$_3$·3H$_2$O, FeF$_3$·0.33H$_2$O/C, and FeF$_3$/C composite are illustrated in Fig. 12. An intercept at the Z' axis in high frequency corresponds to the ohmic resistance (R_s), which represents the resistance of the electrolyte and electrode material. The semicircle in the middle frequency range indicates the charge transfer resistance (R_{ct}). The inclined line in the low frequency represents the Warburg impedance (W_o), which is associated with the diffusion of lithium ions in the solid matrix. A simplified equivalent circuit model (inset) was constructed to analyze the impedance spectra. A constant phase element CPE is placed to represent the double layer capacitance and passive film capacitance. The parameters of the equivalent circuit are recorded in Table 2. It is clear that the R_s of FeF$_3$·0.33H$_2$O/C is 4.268 Ω, which is smaller than FeF$_3$·3H$_2$O/C and FeF$_3$/C. Meanwhile, the R_{ct} of FeF$_3$·0.33H$_2$O/C is 44.99 Ω, which is also the smallest. Therefore, FeF$_3$·0.33H$_2$O/C shows the lowest electrochemical resistant and it has much better charge–discharge properties than other two fluoride samples can be expected.

GITT measurements were performed on the second cycle to determine the diffusion coefficient of Li ions (D_{Li}) in electrode active materials. Fig. 13a–c shows the discharge/charge GITT curves of FeF$_3$·3H$_2$O/C, FeF$_3$·0.33H$_2$O/C, and FeF$_3$/C electrodes as a function of time in the voltage range of 2.0–4.5 V. The test was performed by discharging/charging the cell for an interval of 10 min at a current density of 0.05 C, relaxing 60 min to approach nearly equilibrium state (E_s) and repeating this process in the voltage of 2.0–4.5 V. GITT curves indicate that the overall time of the discharging or charging process of FeF$_3$·0.33H$_2$O/C is longer than that of FeF$_3$·3H$_2$O/C and FeF$_3$/C, suggesting that the capacity of FeF$_3$·0.33H$_2$O/C is the highest among these three samples, which is in consistence with the results (Fig. 10). A single step of GITT at 3.46 V during the discharge process is depicted in Fig. 13d with schematic labeling of different parameters. Fig. 13e shows an example of an E vs. $\tau^{1/2}$ plot recorded for FeF$_3$·0.33H$_2$O/C after application of 0.05x C current pulse. It can be seen that in the time domain from 10 s to 100 s, the plot is roughly linear. In the former researches by using GITT techniques [28–30], the time range of 10–100 s is identical. The slope is taken from this linear range to calculate D_{Li}. Assuming that lithium transport in the electrode obeys Fick's second law, the chemical diffusion coefficients can be obtained by the following equation [30]:

$$D_{Li} = \frac{4}{\pi}\left(I_0\frac{V_m}{SFZ_i}\right)^2\left(\frac{dE/dx}{dE/dt^{1/2}}\right)^2 \quad \left(t \ll L^2/D_{Li}\right) \tag{9}$$

where D_{Li} (cm^2 s^{-1}) is the chemical diffusion coefficient of the mobile specie, V_m (cm^3 mol^{-1}) is the molar volume of the active materials, F is the Faraday constant, I_0 (A) is the applied current, S (cm^2) is the total contact area between the electrolyte and electrodes, Z_i is the number of charge transfer, and L (cm) is the

diffusion length. Based on Equation (9), the diffusion coefficients of Li$^+$ calculated from the GITT curves as a function of cell voltage during cycling are presented in Fig. 13f and g. The size of the data points is within the error limit of estimation.

In the process of Li$^+$ intercalation (see Fig. 11f), the D_{Li} values of FeF$_3$·3H$_2$O/C are in the scope of 1.08 × 10^{-12}–3.12 × 10^{-11} cm^2 s^{-1}, while FeF$_3$/C are in the range of 7.31 × 10^{-12}–1.49 × 10^{-10} cm^2 s^{-1}, and FeF$_3$·0.33H$_2$O/C are in the range of 1.68 × 10^{-11}–3.76 × 10^{-10} cm^2 s^{-1}. In the process of Li$^+$ extraction (see Fig. 13g), D_{Li} values of FeF$_3$·3H$_2$O/C, FeF$_3$·0.33H$_2$O/C and FeF$_3$/C are in the range of 1.30 × 10^{-12}–3.49 × 10^{-11}, 3.60 × 10^{-12}–2.49 × 10^{-10} and 1.35 × 10^{-12}–1.45 × 10^{-10} cm^2 s^{-1}, respectively. Apparently, the D_{Li} of FeF$_3$·0.33H$_2$O/C is the largest, suggesting that FeF$_3$·0.33H$_2$O/C is more favorable to the diffusion of lithium ion and thus has better electrochemical performance than FeF$_3$·3H$_2$O/C and FeF$_3$/C.

4. Conclusions

In summary, FeF$_3$·3H$_2$O/C, FeF$_3$·0.33H$_2$O/C, and FeF$_3$/C nanocomposites have been synthesized by liquid-phase method, followed by ball-milling with conductive acetylene black. The structure, morphology, and electrochemical properties of these three iron fluorides are investigated systematically. XRD and TEM analyses reveal that these three iron fluorides with different hydration water have different crystalline structures. Charge–discharge experiments demonstrate that all the three samples can realize a reversible electrochemical reaction from Fe^{3+} to Fe^0 and vice versa in the voltage of 1.0–4.5 V, as confirmed by CV and XRD evidence. All the three iron fluoride samples have similar electrochemical mechanism, including Li$^+$ insertion/extraction and reversible conversion reaction. Though the specific capacities in the voltage of 1.0–4.5 V are large, which is associated with the three-electron redox, the iron fluorides show poor cycling performance due to the structure disintegration caused by conversion reaction. The electrochemical properties of iron fluorides are drastically improved by raising the cut-off voltage to conduct a simple intercalation/deintercalation reaction. The FeF$_3$·3H$_2$O/C, FeF$_3$·0.33H$_2$O/C and FeF$_3$/C nanocomposites can be well cycled in the voltage of 2.0–4.5 V vs. Li$^+$/Li. This study finds that FeF$_3$·0.33H$_2$O containing trace amounts of crystal water with a typical orthorhombic structure has the best electrochemical performance. FeF$_3$·0.33H$_2$O/C composite delivers an initial discharge capacity of 177.6 mAh g^{-1} at 0.1 C and 105.1 mAh g^{-1} at 5 C, and its capacity retentions remain as high as 83.8% and 83.3% after 100 cycle numbers, respectively. EIS result shows that the electrochemical resistance of FeF$_3$·0.33H$_2$O/C is smaller than those of FeF$_3$·3H$_2$O/C and FeF$_3$/C. GITT tests reveal the FeF$_3$·0.33H$_2$O/C electrode has an excellent Li$^+$ diffusion coefficient during lithiation and delithiation processes. The experimental data demonstrated in this study suggest a potential feasibility to prepare the optimal crystal structure of iron fluorides as high-performance cathode material for lithium-ion batteries.

References

[1] J.B. Goodenough, Y. Kim, Chem. Mater. 22 (2010) 587.
[2] Z.W. Fu, C.L. Li, W.Y. Liu, J. Ma, Y. Wang, Q.Z. Qin, J. Electrochem. Soc. 152 (2005) E50.

[3] Y.L. Shi, M.F. Shen, S.D. Xu, X.Y. Qiu, L. Jiang, Y.H. Qiang, Q.C. Zhuang, S.G. Sun, Int. J. Electrochem. Sci. 6 (2011) 3399.
[4] F. Badway, A.N. Mansour, N. Pereira, J.F. Al-Sharab, F. Cosandey, I. Plitz, G.G. Amatucci, Chem. Mater. 19 (2007) 4129.
[5] M. Nishijima, I.D. Gocheva, S. Okada, T. Doi, J.I. Yamaki, T. Nishida, J. Power Sourc. 190 (2009) 558.
[6] I. Plitz, F. Badway, J. Al-Sharab, A. DuPasquier, F. Cosandey, G.G. Amatucci, J. Electrochem. Soc. 152 (2005) A307.
[7] N. Yamakawa, M. Jiang, B. Key, C.P. Grey, J. Am. Chem. Soc. 131 (2009) 10525.
[8] T. Li, L. Li, Y.L. Cao, X.P. Ai, H.X. Yang, J. Phys. Chem. C 114 (2010) 3190.
[9] H. Li, P. Balaya, J. Maier, J. Electrochem. Soc. 151 (2004) A1878.
[10] R. Prakash, A.K. Mishra, A. Roth, C. Kübel, T. Scherer, M. Ghafari, H. Hahn, M. Fichtner, J. Mater. Chem. 20 (2010) 1871.
[11] R. Prakash, C. Wall, A.K. Mishra, C. Kübel, M. Ghafari, H. Hahn, M. Fichtner, J. Power Sourc. 196 (2011) 5936.
[12] F. Badway, N. Pereira, F. Cosandey, G.G. Amatucci, J. Electrochem. Soc. 150 (2003) A1209.
[13] F. Badway, F. Cosandey, N. Pereira, G.G. Amatucci, J. Electrochem. Soc. 150 (2003) A1318.
[14] F. Cosandey, J.F. Al-Sharab, F. Badway, G.G. Amatucci, P. Stadelmann, Microsc. Microanal. 13 (2007) 87.
[15] C.L. Li, L. Gu, J.W. Tong, S. Tsukimoto, J. Maier, Adv. Funct. Mater. 21 (2011) 1391.
[16] C.L. Li, L. Gu, J.W. Tong, J. Maier, ACS Nano 5 (2011) 2930.
[17] C.L. Li, L. Gu, S. Tsukimoto, P.A. van Aken, J. Maier, Adv. Mater. 22 (2010) 3650.
[18] W. Wu, X.Y. Wang, X. Wang, S.Y. Yang, X.M. Liu, Q.Q. Chen, Mater. Lett. 63 (2009) 1788.
[19] W. Wu, Y. Wang, X.Y. Wang, Q.Q. Chen, X. Wang, S.Y. Yang, X.M. Liu, J. Guo, Z.H. Yang, J. Alloy Compd. 486 (2009) 93.
[20] L. Liu, M. Zhou, X.Y. Wang, Z.H. Yang, F.H. Tian, X.Y. Wang, J. Mater. Sci. 47 (2012) 1819.
[21] L. Liu, M. Zhou, L.H. Yi, H.P. Guo, J.L. Tan, H.B. Shu, X.K. Yang, Z.H. Yang, X.Y. Wang, J. Mater. Chem. 22 (2012) 17539.
[22] C. Wu, X.X. Li, F. Wu, Y. Bai, M.Z. Chen, Y. Zhong, Adv. Mater. Res. 391–392 (2012) 1090.
[23] M.J. Zhou, L.W. Zhao, T. Doi, S. Okada, J.I. Yamaki, J. Power Sourc. 195 (2010) 4952.
[24] R.K. Hocking, S.G. DeBeer, K.N. Raymond, K.O. Hodgson, B. Hedman, E.I. Solomon, J. Am. Chem. Soc. 132 (2010) 4006.
[25] P. Liu, J.J. Vajo, J.S. Wang, W. Li, J. Liu, J. Phys. Chem. C 116 (2012) 6467.
[26] S.W. Kim, D.H. Seo, H. Gwon, J. Kim, K. Kang, Adv. Mater. 22 (2010) 5260.
[27] S.T. Myung, S. Sakurada, H. Yashiro, Y.K. Sun, J. Power Sourc. 223 (2013) 1.
[28] R. Amin, J. Maier, P. Balaya, D.P. Chen, C.T. Lin, Solid State Ionics 179 (2008) 1683.
[29] S.T. Coleman, W.R. McKinoon, J.R. Dahn, Phys. Rev. B 29 (1984) 4147.
[30] W. Weppner, R.A. Huggins, J. Electrochem. Soc. 124 (1977) 1569.